# Imaging strain localization by X-ray computed tomography: discrete compaction bands in Diemelstadt sandstone

Laurent Louis [a,*], Teng-fong Wong [a], Patrick Baud [b], Sheryl Tembe [a]

[a] *Department of Geosciences, State University of New York at Stony Brook, Stony Brook, NY, 11794-2100, USA*
[b] *Institut de Physique du Globe (CNRS/ULP), 5 rue Descartes, 67084 Strasbourg, France*

## Abstract

Compaction localization was observed in Diemelstadt sandstone during triaxial experiments over a broad range of effective pressures (60–165 MPa). High resolution X-ray CT imaging was used to resolve the 3D the geometry of the localization features developed as tabular bands subperpendicular to the maximum compressive stress. While the raw X-ray attenuation data provide very low contrast between relatively intact and deformed areas as opposed to similar studies involving dilatancy, skewness (asymmetry of the distribution of attenuation values) and local standard deviation were demonstrated to be useful in locating and delineating the complex geometry of the compacted zones. Complementary microstructural study including damage mapping confirmed the observed features as compaction bands. Geometric attributes such as average thickness, tortuosity and orientation were evaluated from the CT data. Our study underscores the advantage of working with an image resolution of about 0.1 mm in granular media, which is intermediary to synchrotron ($\sim 1$ µm) and conventional medical CT (1 mm) resolutions. Our methodology can be used for imaging other compactant localization features, such as compactive shear bands and diffuse compaction bands in naturally deformed samples, provided that the undeformed rock does not possess preexisting heterogeneities comparable with those expected from compaction localization.
© 2006 Elsevier Ltd. All rights reserved.

*Keywords:* Compaction localization; Sandstone; Microscopy; X-ray computed tomography; Density distribution; Image processing

## 1. Introduction

Strain localization is a deformation and failure phenomenon that is pervasive in the Earth's crust over a broad range of length scales. It occurs in cm-sized laboratory samples all the way up to crustal fault zones extending over hundreds of kilometers. Since localized deformation can significantly influence the stress field, strain partitioning and fluid transport, it is important to have a fundamental understanding of the mechanics of strain localization and its impact on permeability. Shear and extensile discontinuities in the forms of faults and joints have been investigated thoroughly in the field and laboratory. These phenomena are accompanied by dilatancy, and accordingly attention has previously focused on strain localization associated with dilatant failure in crystalline and sedimentary rocks (e.g. Segall and Pollard, 1983; Willemse et al., 1997). However, strain localization associated with

compactant failure has recently become a focus of research, motivated by a number of geologic (Mollema and Antonellini, 1996) and laboratory (Olsson and Holcomb, 2000; Baud et al., 2004) observations of compaction localization, primarily in porous sandstones.

Laboratory studies under controlled conditions of stress and pore pressure have provided useful insights into the mechanics of strain localization (Paterson and Wong, 2005). The mechanical data constrain the constitutive parameters, which can then be incorporated into a theoretical model to predict the onset of strain localization (Bésuelle and Rudnicki, 2004; Borja and Aydin, 2004). While such an analysis is useful in describing the phenomenology, before one can extrapolate and compare with structural geology observations it is essential to also have complementary observations on the deformation mechanisms and geometric complexity associated with the development of strain localization. Conventionally such observations are conducted using optical or scanning electron microscopes on thin-sections of failed samples (e.g. Tapponier and Brace, 1976; Wong, 1982; Menéndez et al., 1996; DiGiovanni et al., 2000; Bésuelle et al., 2003; Baud et al., 2004). These microstructural analyses have elucidated

---

* Corresponding author.
  *E-mail address:* llouis@notes.cc.sunysb.edu (L. Louis).

the grain-scale damage processes and micromechanics of localized failure, but the 2D observations are limited in their capability to resolve the geometric complexities, which would require the use of acoustic emission (AE) measurements and 3D imaging techniques.

By observing the relative arrival times of the AE pulses at multiple transducers attached to the surface of a specimen under stress, the spatial origin of the damage can be located. Such AE measurements can map out in 3D the spatio-temporal evolution and localization of damage during either dilatant (Lockner et al., 1992) or compactant (Olsson and Holcomb, 2000; Fortin et al., accepted) failure. Using transducers with frequency responses in the MHz range the location of AE hypocenters in typical crustal rock has an accuracy of $\sim 2$ mm (Lockner, 1993). Since grain-scale damage processes are operative on the sub-mm scale, AE focal mechanism solutions do not have the spatial resolution to unambiguously identify these micromechanical processes and therefore it is important to incorporate 3D imaging with finer resolutions to provide the supplementary information.

X-ray computer tomography (CT) is a nondestructive technique for 3D imaging that has recently been used in many geological applications. It maps out the spatial distribution of X-ray attenuation, which increases with increasing atomic number and decreasing porosity. In recent years significant advances have been made in the spatial resolution of CT imaging. Whereas conventional CT in medical systems typically have a rather coarse resolution on the order of 1 mm, microtomography using synchrotron X-ray sources are now capable of imaging mm-sized samples with spatial resolution on the order of 1 µm (Flannery et al., 1987; Coles et al., 1998; Lindquist et al., 2000). Realistic simulation of fluid transport can now be conducted on the basis of such data on the fine-scale structure and geometric complexity of the pore space (Auzerais et al., 1996; Arns et al., 2004; Renard et al., 2004; Fredrich et al., 2006).

In contrast, relatively little research has been performed using either 'industrial' CT (with resolution $\sim 0.1$ mm) or microtomography to map out damage distribution in deformed and failed rock samples. Nevertheless published studies using medical CT have demonstrated the potential of 3D imaging for characterizing the damage evolution, especially in relation to shear localization during dilatant failure (e.g. Raynaud et al., 1989; Kawakata et al., 1999; Bésuelle et al., 2003), but also in naturally compacted sandstone (Antonellini et al., 1994; Aydin et al., 2006). However, while dilatancy enhances the local porosity and is very effective in increasing the contrast in X-ray attenuation between a dilating shear band and its surroundings, localized compaction obtained experimentally is not as effective and the resulting contrast is appreciably less between a compacted zone and its surroundings. Consequently the geometry of compaction bands cannot be resolved simply by 3D visualization of the primary data in the form of CT values. In this paper we developed a methodology whereby the spatial distribution of compactant damage can be extracted from the CT data.

Our technique hinges on the hypothesis that inelastic compaction in a porous sandstone (primarily involving grain

crushing and pore collapse) would homogenize the spatial distribution of X-ray attenuation, and accordingly the local damage intensity can be inferred from the relative dispersion of the CT-value in an elemental volume made up of multiple voxels. We considered a cubic volume with linear dimension comparable with the average grain size, and acquired CT data at a spatial resolution such that this elemental volume comprises $3^3$ voxels. Diemelstadt sandstone samples were deformed under pressure conditions favorable for the development of discrete compaction bands (Baud et al., 2004). Statistical analysis of the CT data for such a failed Diemelstadt sandstone sample supports our hypothesis, in that the standard deviation and relative dispersion of the CT-value in an elemental volume was observed to be appreciably lower for crushed grains inside a localized compaction band than for less damaged grains outside. We also conducted microstructural observations to investigate the micromechanical processes possibly responsible for homogenizing the grain-scale X-ray attenuation. By mapping out the relative dispersion, we quantitatively characterize geometric attributes such as the thickness and tortuosity of compaction bands in the Diemelstadt sandstone.

## 2. Sample preparation and X-ray computed tomography

Diemelstadt is the name of a German quarry. The Diemelstadt sandstone is a fluvial sandstone belonging to the (Triassic) Buntsandstein formation. It has a nominal porosity of 24.3% and average grain radius of 80 µm. Its modal composition is 68% quartz, 26% feldspar, 2% micas, and 4% other minerals (mostly oxides) (Klein and Reuschlé, 2004). Our samples were cored perpendicular to the sedimentary bedding from the same block as that studied by Baud et al. (2004). The samples were cylindrical, with diameter 18.4 mm and length 38.1 mm. Our mechanical data and microstructural observations indicate that there is a subset of samples showing bedding laminations. These were not considered in this study, which focused only on macroscopically homogeneous samples.

Following the methodology of Wong et al. (1997), experiments were conducted on samples saturated with distilled water under drained conditions at fixed pore pressure of 10 MPa and nominal axial strain rate of $1.3 \times 10^{-5}$ s$^{-1}$. The tests were performed in the conventional triaxial configuration at room temperature. After the deformed samples were unloaded and retrieved from the pressure vessel, the jackets were carefully removed and the samples were exposed to the atmosphere for several weeks.

The nominally dry samples were then sent to the High-Resolution CT Facility at the University of Texas at Austin for imaging following the approach described by Ketcham and Iturrino (2005). The ultrahigh-resolution system employs a 200 kV microfocal X-ray source capable of a $< 10$ µm focal spot size. Our data were obtained with the source at a peak energy of 180 kV, and each rotation consisted of 1600 views (angular positions). The data were captured via a CCD $1024 \times 1024$ camera, and the in-plane resolution and slice spacing are

such that each voxel is a cube with a linear dimension of 48.78 μm. After correcting for beam hardening and ring artifacts, the X-ray intensity was converted to a CT-value, which maps linearly the effective attenuation coefficient of the material in each voxel (Ketcham and Carlson, 2001).

Since X-ray attenuation increases with increasing atomic number (if it is predominately due to photoelectric and Compton effects), the CT-value in a porosity-free material is dependent on the solid grain mineralogy, whereas in a porous rock the void space significantly perturbs the attenuation within a voxel and accordingly the CT-value can be used to infer the spatial distribution of porosity (Wellington and Vinegar, 1987; Ketcham and Carlson, 2001). Indeed calibrations performed on porous rocks and soils (Vinegar et al., 1991; Desrues et al., 1996) have established a linear relationship between X-ray attenuation and local density. Typically, the reconstruction parameters are optimized so that the data would fill up the available gray-scale range. In our data set this range of gray level (16 bit or 0–65535) was optimized so that it roughly extends from the CT-value of air to the value of the densest mineral present in the sandstone. An estimate of the correspondence between gray level values and actual densities can be obtained by using the average gray level value for areas outside the sample (air, ∼5000 gray level units) and for the sample (∼25000 gray level units). Assuming density values of 0 and 2, respectively, a linear relationship can be drawn. Fe oxides with densities close to 5 are therefore expected to return values around 55000 gray level units.

## 3. Mechanical data and failure mode

In this paper we will use the convention with the compressive stresses and compactive strains taken as positive. We will denote the maximum and minimum (compressive) principal stresses by $\sigma_1$ and $\sigma_3$, respectively. The pore pressure will be denoted by $P_p$, and the difference $P_c - P_p$ between the confining pressure ($P_c = \sigma_2 = \sigma_3$) and pore pressure will be referred to as the 'effective pressure' $P_{eff}$. The effective mean stress $(\sigma_1 + 2\sigma_3)/3 - P_p$ will be denoted by $P$ and the differential stress $\sigma_1 - \sigma_3$ by $Q$.

We performed a total of 15 experiments at effective pressures ranging from 10 to 165 MPa, which was sufficiently broad for the failure mode to go through the brittle–ductile transition. All the failed samples were impregnated with epoxy and then sawn along a plane parallel to the axial direction to prepare petrographic thin-sections. The optical microscopy observations provide complementary information for analyzing the CT data. Selected thin-sections were also sputter-coated with 3 nm of gold and studied using a LEO 1550 scanning electron microscope (SEM). The SEM micrographs were acquired as backscattered electron images at a voltage of 15 kV.

Mechanical data illustrating the development of localized compactive failure are presented in Fig. 1, for sample Di13 deformed at 160 MPa confining pressure and 10 MPa pore pressure. Differential stress and acoustic emission (AE) activity are plotted as functions of the axial strain in Fig. 1a. AE activity is reported as a number of events per second. The stress–strain curve displays an overall strain hardening trend punctuated by small stress drops, with corresponding episodic surges in AE rate. The effective mean stress as a function of porosity change is shown in Fig. 1b. If porosity change is solely controlled by the effective mean stress and independent of the differential stress, the triaxial data (solid curve) for Di13 in Fig. 1b should coincide with a hydrostatically compressed sample (shown as the dashed curve). Indeed the two curves coincide up to a critical stress state (marked as $C^*$), beyond which there was an accelerated decrease in porosity in comparison with the hydrostat. At stress levels beyond $C^*$ the deviatoric stress field provided a significant contribution to the compactive strain, and this phenomenon of inelastic yield by 'shear-enhanced compaction' (Wong et al., 1997) is
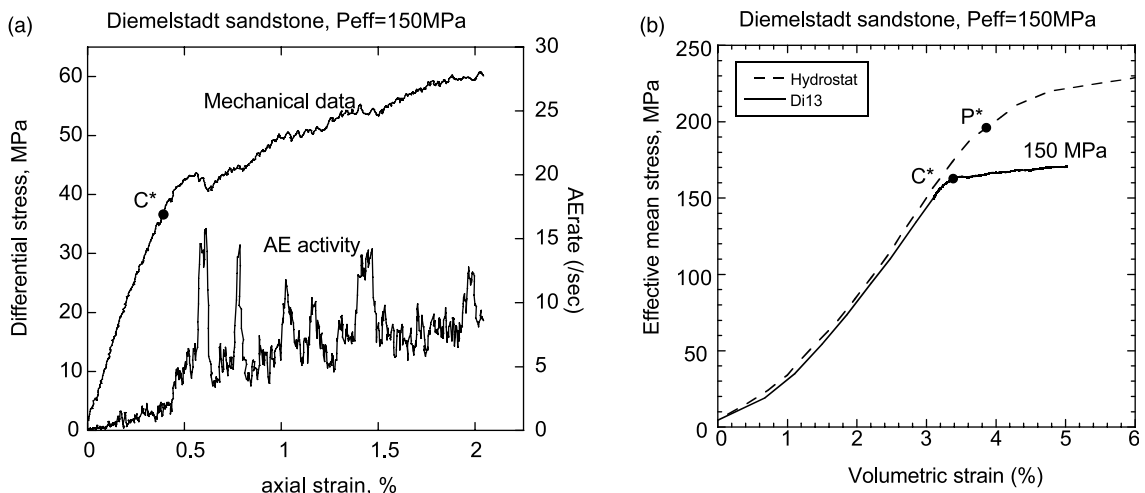


Fig. 1. Mechanical data for sample Di13. (a) Principal stress difference and rate of acoustic emissions versus axial strain for triaxially compressed sample of Diemelstadt sandstone at 150 MPa effective pressure. The stress–strain curve displays an overall strain hardening punctuated by stress drops, with corresponding episodic surges in AE rate. (b) Effective mean stress versus volumetric strain in Diemelstadt sandstone. For reference, the hydrostat is shown as a dashed curve. The initial yield stress $C^*$ for onset of shear-enhanced compaction and critical pressure $P^*$ for onset of grain crushing and pore collapse are also marked.

attributed to the inception of grain crushing and pore collapse in the sandstone (Menéndez et al., 1996).

In the following discussion of localized failure mode we will adopt the classification of deformation bands presented recently by Aydin et al. (2006). A deformation band is classified kinematically as a 'shear' or 'volumetric' deformation band according to whether the localized deformation is predominantly achieved by shearing or volume change. The localized deformation in a shear band may involve a certain amount of volume increase or decrease, and accordingly these bands can be further distinguished as either 'compactive' or 'dilatant' shear bands. If a volumetric deformation band was solely subjected to volume reduction or expansion, it is called a 'compaction band' or 'dilation band'. Moreover, using the terminology introduced by Baud et al. (2004) on the basis of their data for five sandstones with porosities ranging from 13 to 24%, a localized structure that has a thickness of only a few (say $\leq 3$) grains is referred to as a 'discrete band', whereas thicker structures are called 'diffuse band'.

Our data for Diemelstadt sandstone show that compactant failure occurred predominantly by the development of compaction bands, which were observed in deformed samples at effective pressures from 60 to 165 MPa. Our experiment on Di13 was terminated at a final axial strain of 2.0% (Fig. 1a). To illustrate the failure mode and its development, we show in Fig. 2a and b the thin-sections of two samples (Di14 and Di7) deformed at the same effective pressure (150 MPa) to axial strains of 1.6 and 3.0%, respectively. Relatively dark bands subperpendicular to $\sigma_1$ can be discerned in these thin-sections. The SEM observations reveal details of the pore geometry and damage in sample Di7. Fig. 2c shows a relatively undamaged area outside the bands, and Fig. 2d shows the intense grain crushing and Hertzian fracturing inside one of these bands, which typically have thicknesses of three grain diameters or so. These relatively dark bands in the thin-sections correspond to discrete compaction bands, and comparison of Fig. 2a and b shows that more bands have developed in the sample with larger strain. Since the strain in sample Di13 was intermediate between Di14 and Di7, one would expect also the density of discrete bands in Di13 to be in between these samples. Similar microstructural observations were documented by Baud et al. (2004) in the Bentheim sandstone, where intense grain crushing was already considered as a proxy for the development of compaction localization, making the implicit assumption that there is a one-to-one correspondence between discrete zones of intense cataclasis and volumetric loss.

## 4. CT Imaging of compaction bands in Diemelstadt sandstone

The failed sample Di13 was first imaged using X-ray CT before it was cut to prepare a thin-section. Fig. 3a is a digital photograph of the exterior surface of the sample, on which one can discern several light bands that have developed sub-perpendicular to the $\sigma_1$ direction. The material these bands are made of readily chipped off when we removed the copper jacket on the sample. We inferred that these correspond to compaction bands, which appear lighter in color possibly due to fresh surfaces exhibited by the damaged grains.

CT measurement of X-ray attenuation by itself is not very effective for differentiating a discrete compaction band from its surroundings in the Diemelstadt sandstone. Fig. 3b shows our CT data for a vertical slice passing through the central axis. Extrapolating from the trace of a light band on the exterior surface we infer that if indeed the compaction band had propagated across the sample, then a layer of crushed grains is probably embedded in area 2 marked in Fig. 3b. Due to pore collapse compactant damage is expected to be associated with lower porosity and higher attenuation, thus the compaction band would have higher CT-value (or gray level) and appear lighter in the image. However, such a light band cannot be readily identified on the CT image in Fig. 3b.

It was concluded that we need to identify alternative parameters (which can be derived from the CT-value) that
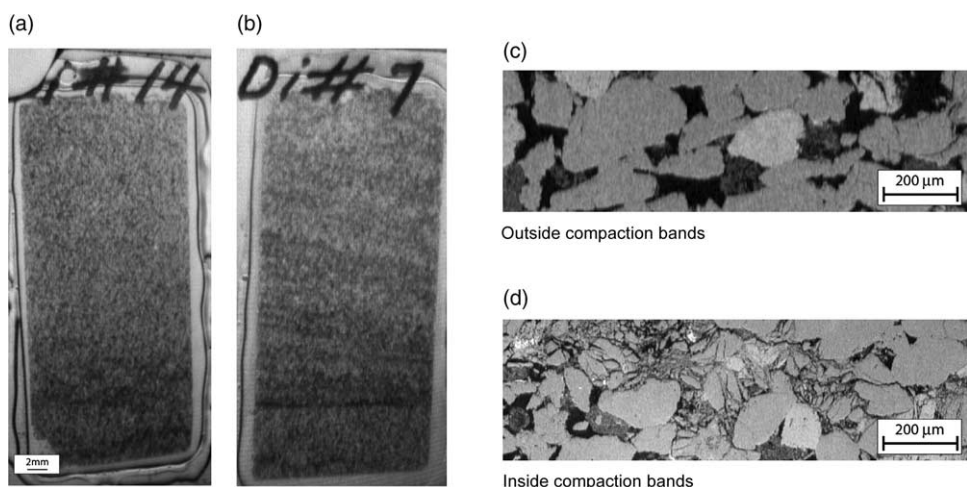


Fig. 2. (a) and (b) Thin sections of samples of Diemelstadt sandstone triaxially deformed at 150 MPa effective pressure up to axial strain 1.6% (Di14) and 3% (Di7), respectively. Compaction bands appear as relatively dark areas. Note the increasing number of bands with increasing strain. (c) Detail of a SEM picture in a relatively intact area of the Diemelstadt sandstone. (d) SEM picture taken inside a compacted area. The image shows intense grain crushing and Hertzian fracturing. Pore size was also considerably reduced as compared with (c).

(a)　　　　　　　(b)

(c)

Whole image

Mean: 24886
σ: 1863
σ/mean: 0.075

16 bit grey level

(d)

Mean　σ
Area 1: 24902 1829
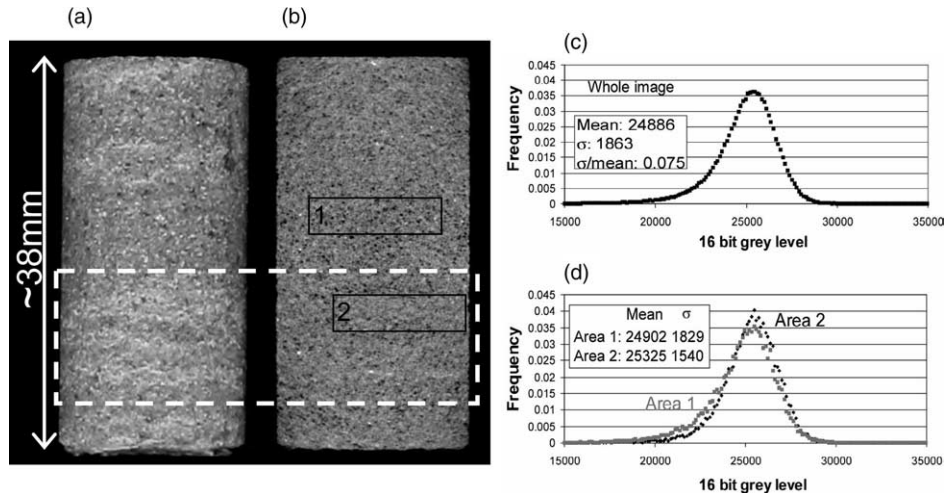Area 2: 25325 1540

Area 2

Area 1

16 bit grey level

Fig. 3. (a) Photograph of the sample Di13 after triaxial testing at 150 MPa effective pressure. Light bands made of crushed material have developed on the exterior surface subperpendicular to the $\sigma_1$ direction. (b) CT data for a vertical slice passing through the central axis. Extrapolating from the trace of a light band in (a), area 2 probably includes a layer of crushed grains while area 1 appears relatively undeformed. (c) Distribution of X-ray attenuation values (0–65535) for the whole slice in Fig. 2b. (d) Distribution of X-ray attenuation values for areas 1 and 2. The distribution in area 1 is more skewed than in area 2 because of a higher fraction of low gray levels. Also, distribution in area 2 is narrower than in area 1, which corresponds to a lower standard deviation.

show appreciable contrast in values inside and outside a compaction band. Our search for such parameters was guided by the statistical variation of CT-value. Fig. 3c shows the frequency data for the gray level of all the pixels of the vertical slice, which can be described as approximately normal. From the appearance of the exterior surface we inferred that area 2 in Fig. 3b is associated with localized compaction while area 1 is relatively undamaged. Fig. 3d shows the frequency data for the CT-values in areas 1 and 2. It can be seen that area 2 has a slightly higher mean value indicative of lower porosity and higher density. However, the difference in mean values between areas 1 and 2 is relatively small when compared with the width of the statistical variation, which explains why it is difficult to resolve the compacted zones solely on the basis of the gray level or CT-value. Nevertheless two appreciable differences between the statistics for areas 1 and 2 can be noted from Fig. 3d. First, the distribution for area 1 is more skewed because a higher fraction of the voxels have low gray levels, corresponding to regions of relatively low density (and high porosity). Second, the distribution for area 2 is narrower and consequently its standard deviation is considerably lower than area 1. Motivated by these observations we decided to use the skewness and coefficient of variation as proxies for damage and porosity reduction.

### 4.1. Skewness as a measure of porosity reduction in a band

Our SEM observations indicate that in relatively undamaged areas outside the compaction bands there are a number of pores with dimensions comparable with the voxel width (48.78 μm) (Fig. 2c). If one of these larger pores is embedded in a voxel, then its CT-value (and gray level) will fall on the tail of low values in the distribution curve. However, our SEM observations also show that due to grain crushing and pore collapse most of the larger pores had been eliminated and very few pores with dimensions comparable with the voxel width could be found within a compaction band (Fig. 2d). This implies that the distributions of CT-values in a band (such as area 2 in Fig. 3b) would have short tails on the low-value end, rendering the distributions to be less skewed.

To use the skewness for highlighting porosity reduction within compaction bands, we consider an elemental band with axial length equal to 10 pixels (489 μm, or about 3 grains). The bands were assumed to have uniform width extending laterally across the section. For each elemental band we evaluated the mean value $\mu$, mode $M$ and standard deviation $\sigma$. Once these parameters had been evaluated, the elemental band was shifted along the axial direction by one pixel, and the calculation repeated. The skewness was then determined by $(\mu - M)/\sigma$. Depending on whether the asymmetry of the distribution extends to the right or to the left hand side of the distribution, skewness may take, respectively, negative or positive values. High porosity areas should be associated with more negative skewness while compacted areas are associated with more positive skewness. The axial variation of skewness for a vertical slice is shown in Fig. 4a. One can readily identify a number of intervals with relatively high skewness. The result of this 1D approach is shown in Fig. 4b, with high positive values of skewness shown as relatively light bands. The two arrows bracket an area of high skewness corresponding to area 2 in Fig. 3b.

This approach is relatively simple to implement, and it demonstrates the potential of using first-order features of the CT-value statistics to map out strain localization. However, we incorporated the idealized assumption that the compaction bands are planar features that cut through the section because it was necessary to have a relatively large population of CT-values to obtain a meaningful estimate of the skewness, and accordingly only one geometric parameter (the average band thickness) can potentially be extracted from our analysis.
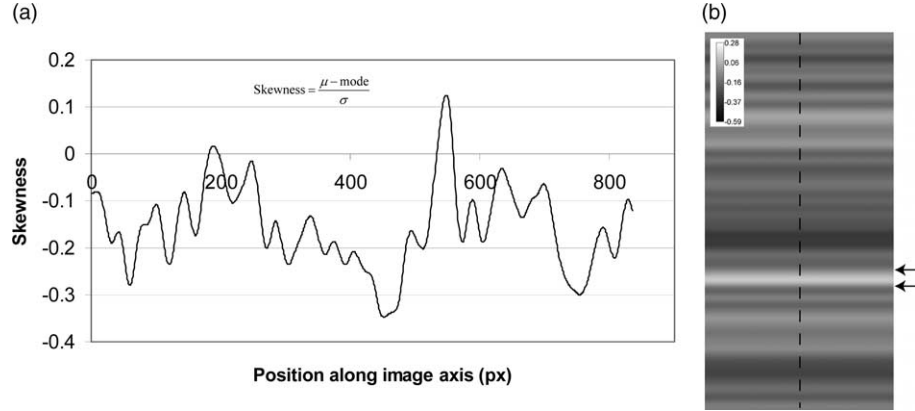
(a)

(b)



Fig. 4. (a) Variation of the skewness parameter across a vertical profile on Fig. 3b. One can readily identify a number of intervals with relatively high skewness. (b) Result of the 1D model. Alternating areas of more negative and more positive skewness match higher and lower porosity areas in Fig. 3b.

## 4.2. Coefficient of variation as a local measure of damage induced by grain crushing and pore collapse

It is likely that relative movement of the crushed grains and pore collapse have eliminated some of the larger pores in a compaction band and resulted in a narrower pore size distribution, which is manifested by a narrower distribution of CT-value. This suggests the use of relative dispersion of X-ray attenuation as a local measure of damage. Specifically we consider an elemental volume made up of $3^3$ voxels

(Fig. 5a). Each side of the cube has a length of 0.15 mm, which is almost identical to the average grain diameter of 0.16 mm. For each elemental volume we evaluated the mean value $\mu$ and standard deviation $\sigma$ of the ensemble of 27 CT-values. Once evaluated, the elemental volume was shifted in one of the three directions by one pixel, and the calculation was repeated. These calculated values are reported as the mean and standard deviation at the mid-point of the innermost voxel of the elemental volume. The coefficient of variation (or coefficient of dispersion) is then defined by $\delta = \sigma/\mu$.

## Local

(a)

$$\sigma = \sqrt{\frac{\sum_i (x_i - \mu)^2}{N-1}}$$
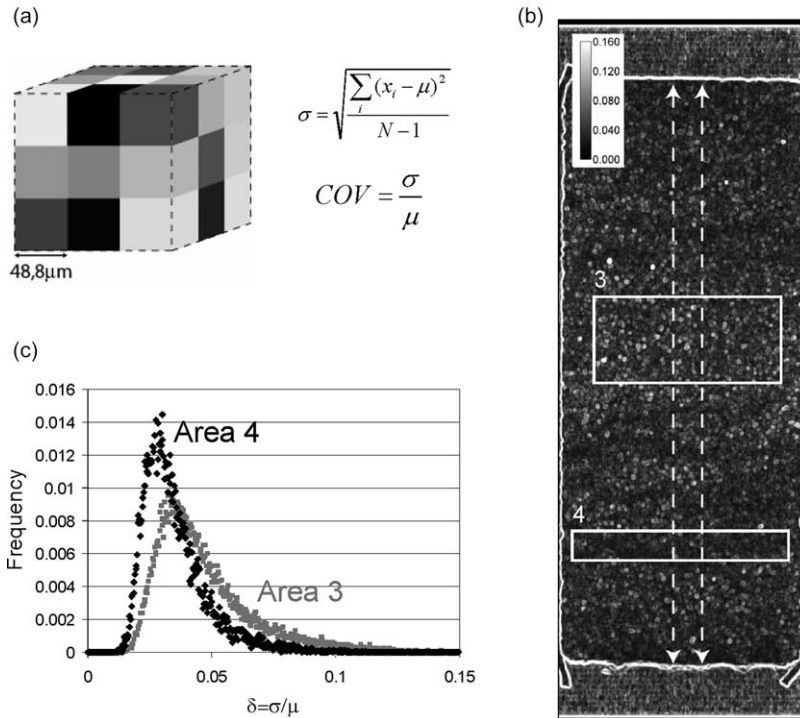
$$COV = \frac{\sigma}{\mu}$$

48,8μm

(c)

(b)



Fig. 5. (a) Elemental volume made up of 27 voxels used for the calculation of the local value of the coefficient of variation $\delta$. Each side of the cube has a length of 0.15 mm, which is almost identical to the average grain diameter of 0.16 mm. (b) Spatial distribution of the coefficient $\delta$ on a vertical slice. The contrast between bands, of which one falls in area 4, and relatively undamaged areas was significantly enhanced. (c) Distribution of $\delta$ value in areas 3 and 4. The mean value in area 4 (0.035) is significantly lower than in area 3 (0.046). The higher dispersion in area 3 may correspond to the presence of large pores of size comparable with the voxel size.

We show in Fig. 5b the spatial distribution of the coefficient $\delta$ on a vertical slice. The resulting contrast was significantly enhanced to the extent that one can readily identify a number of somewhat tortuous dark bands (with lower $\delta$ values). One such band falls in the area marked as 4 in Fig. 5b. The statistical distribution of the coefficient $\delta$ among 31496 pixels in the relatively undamaged area 3, and 12312 pixels in area 4 are shown in Fig. 5c. In the latter area the mean value of $\delta$ is 0.035, which is significantly lower than the mean value of 0.046 in area 3. Furthermore the range of the coefficient of variation is much narrower in area 4. The relatively undamaged area 3 has many elemental volumes with very high dispersion, which possibly correspond to volumes that include large pores with dimensions comparable with the voxel size and are therefore expected to have very high contrast in CT-value among voxels within an elemental volume.

Using the dispersion coefficient as a local measure of damage we were able to map out what we inferred to be the spatial distribution of compaction localization and the geometric complexity of compaction bands in the third dimension. This is illustrated in Fig. 6b, which shows six serial sections for the rectangular area marked in white in Fig. 6a. A number of dark tortuous bands were observed to cut across the sample section, emanating from traces of light bands seen on the exterior surface that were inferred to be compaction bands. Fig. 7 presents the raw data of gray level and dispersion coefficient as functions of axial distance along the two traverses indicated in Fig. 5b. Up to eight local minima in the coefficient $\delta$ (bracketed between the two dashed lines) can be identified, which would otherwise be difficult to pick out from the raw CT-data. To validate that these local minima indeed correspond to intensely damage zones inside discrete compaction bands, we conducted parallel observations on

a thin-section of the failed sample that was prepared after Di13 had been scanned.

### 4.3. Comparison with microstructural observations

Fig. 8a is a general view of the section observed in transmitted light. Compaction bands can be discerned as relatively dark areas. The rectangular area marked in this figure (which overlaps with part of the serial section at depth $X = 9.1$ mm in Fig. 6b) is shown under higher magnification in Fig. 8b. One can observe three relatively dark bands showing intense grain crushing. Fig. 8c shows in further detail the damage morphology typical of Hertzian fracturing (similar to that in Fig. 2d) and the rapid transition from relatively undamaged to intensively crushed material over 3 grain diameters or so.

To quantify the spatial distribution of damage (on the rectangular area marked in Fig. 8a) we followed Menéndez et al. (1996) to define a damage index ranging from I to IV. The rectangle was subdivided into elemental squares 500 μm wide, and the crack density in each square (defined as average number $n$ of cracks per grain) was characterized under the optical microscope. The damage index has a value of I for an elemental square with $0 \leq n < 2$, II for $2 \leq n < 5$ cracks, III for $5 \leq n < 10$ cracks and IV for $n \geq 10$. Fig. 9a shows the damage index data. It can be seen that highly damaged zones corresponding to an index of IV are rarely thicker than the width of one elemental square (i.e. 500 μm), and if we were to define compaction bands by elemental areas with damage indices of III and IV then three bands can be recognized cutting across the section. Since the damage index scale with only four values was relatively coarse, it is difficult to visualize the bands as continuous features from the raw data. To better visualize
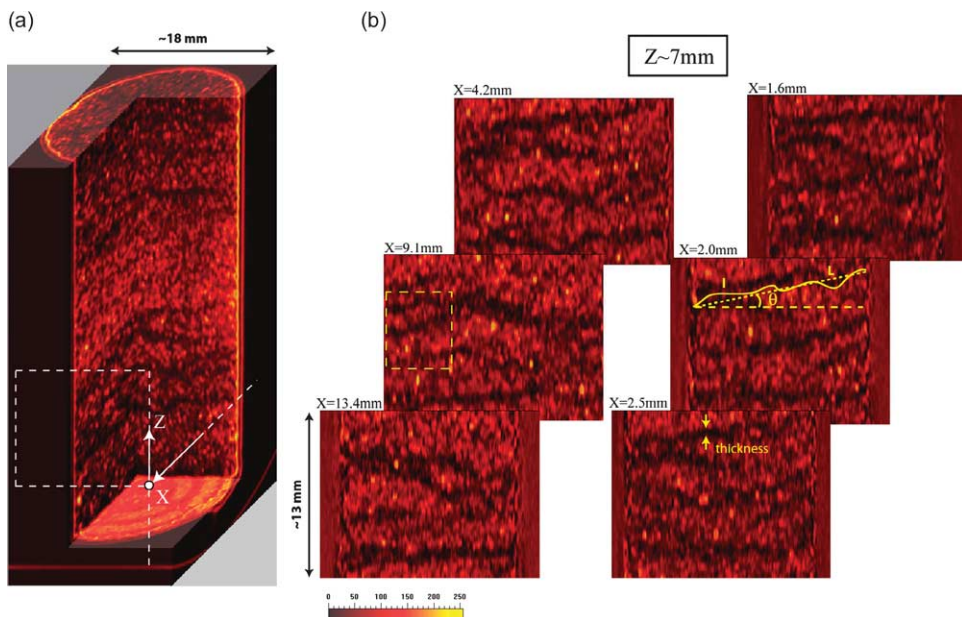


Fig. 6. (a) 3D block reconstruction of the deformed sample Di13 in terms of $\delta$ values. A number of dark tortuous bands emanating from traces of light bands seen on the exterior surface in Fig. 3a cut across the sample. (b) Six serial sections for the rectangular area marked in white in (a). These images show the complex geometry of compaction bands in the third dimension.
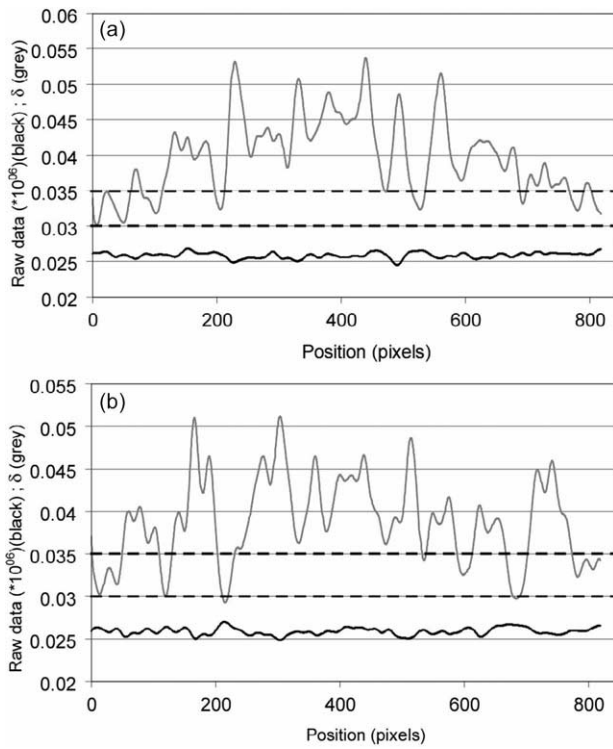
Fig. 7. Raw data of gray level (black) and dispersion coefficient (gray) as a function of axial distance along the two traverses indicated in Fig. 5b. Up to eight local minima in the coefficient δ can be identified, which would be difficult to pick out from the raw CT data.

the bands for comparison with the CT data (which has a much wider range of gray scales) we first applied a Gaussian filter with a radius of one pixel to the damage index map and then resized the image by a factor of 10 by linear interpolation. The filtered image in Fig. 9b shows three light bands (with high damage index) with an overall geometry that corresponds very well to the dark bands (with low coefficients of variation) highlighted in the serial section shown in Fig. 6b. This kind of comparison was performed for a number of randomly selected

areas on the thin-section, which confirms the overall agreement between intensely damaged zones (from microstructural observation) and bands corresponding to localized minima of the dispersion coefficient δ (from CT-data).

### 4.4. CT image binarization and characterization of geometric attributes of compaction bands

Before we can characterize quantitatively the geometric attributes of the discrete compaction bands, it is necessary to first binarize the CT images. The microstructural observations show a significant increase in damage while the and the CT data show an appreciable decrease in dispersion coefficient as one traverses from outside to inside a compaction band. However, these are not discontinuous changes and therefore to binarize the continuous gray-scale data one needs to impose a threshold criterion. Our experience has shown that for this type of analysis an 8-bit image (with gray scale 0–255) would provide sufficient details and the geometric attributes can be extracted without overly intensive computation. An upper threshold value was chosen and voxels with dispersion coefficients δ lower than the threshold value were considered to belong to a compaction band. Guided by our microstructural observations and through trial and error, we conducted three evaluations with threshold gray-level values of 30, 40 or 50, corresponding approximately to δ values of 0.03, 0.032 and 0.035, respectively. The two extreme values (0.030 and 0.035), which are represented by dashed lines in Fig. 7, were chosen so that they largely cover the domain in which the boundary between compaction bands and their surrounding could be picked.

Fig. 10a shows one of these binarized image for a portion of the section at $X = 9.1$ mm (Fig. 6b) using an upper threshold of gray level 40. On the image there are some very small clusters that may represent incipient compaction zones, but since our focus was on well-developed compaction bands we decided not to include such small clusters. If an isolated cluster had an area less than 200 pixels it would be excluded. The image obtained
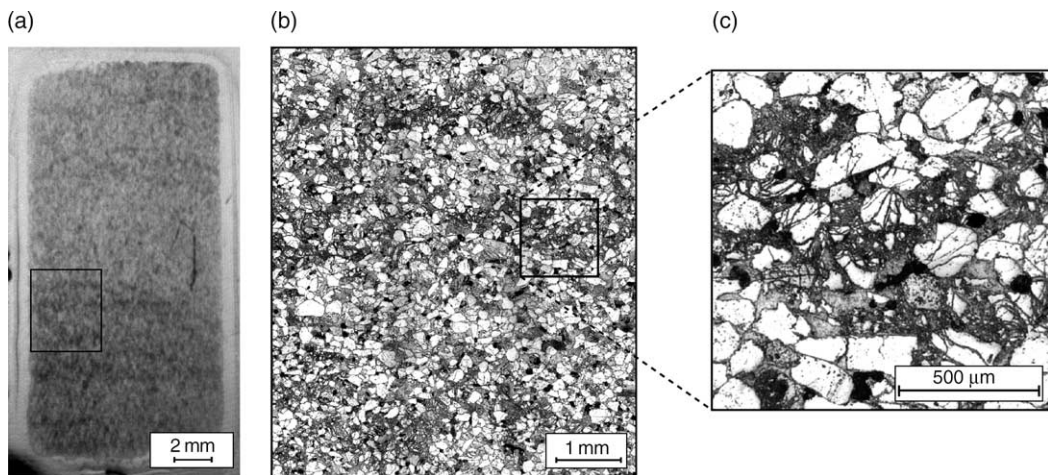


Fig. 8. (a) General view of a thin section of sample Di13 after deformation at 150 MPa effective pressure. Compaction bands are discerned as relatively dark areas. (b) Closer view of the rectangular area in (a). Darker bands show intense grain crushing. (c) Further detail of a compaction band. Damage morphology is typical of Hertzian fracturing and the transition from relatively undamaged to intensively crushed material is very rapid. The band width spans over 3 grains or so.
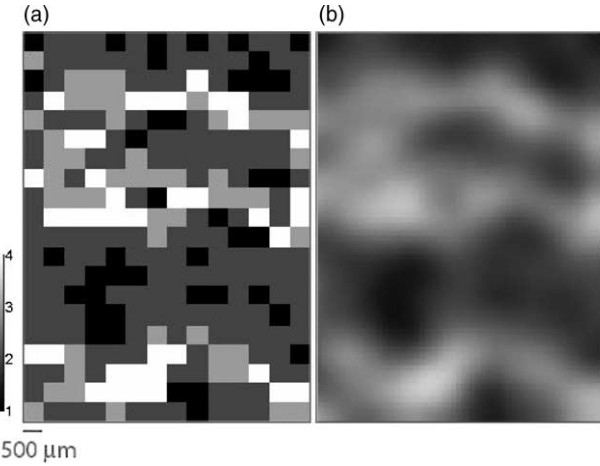
Fig. 9. Damage map developed from thin section analysis over area covered by Fig. 8b. (a) Damage index data. Damage index varies from I (0–2 cracks per grain) to IV (over 10 cracks per grain). Three bands appear to be cutting across the section. (b) Same image as (a) smoothed with a Gaussian filter of radius 1 pixel and resized by a factor of 10 by linear interpolation. The result shows three light bands with a geometry that corresponds very well with the dark bands in Fig. 8b.

after this second step of filtering (Fig. 10b) was used for characterizing of the thickness of the compaction bands.

To determine approximately the thickness of a band at a given location on a 2D section we counted the number of contiguous pixels in the axial direction (Fig. 6b). Fig. 11a shows the width distribution so characterized for 110 images taken near the axial section of the sample. The three curves represent data from images binarized using threshold gray level values of 30, 40, and 50. As expected, a larger population is associated with the images binarized using a higher threshold. Notwithstanding the different thresholds adopted in these analyses, we obtained a rather robust estimate of the most frequent band thickness. As shown in Fig. 11a the modes of these width distributions fall in the rather narrow range of 10–11 pixels, corresponding to compaction band thickness of 490 and 540 μm, respectively (between 3 and 4 grain diameters). This estimate is not very sensitive to the particular choice of the threshold.

Taking an average band thickness at $l = 515$ μm and inferring from Fig. 7 a number of bands $n = 8$, we can estimate the porosity reduction inside a discrete compaction band.

The inelastic axial strain in the failed sample was 0.015, which corresponds to a shortening of $\Delta l = 570$ μm, and if we assume that this strain was equally distributed among the eight bands, then the inelastic axial strain localized in each band is given by $\varepsilon^{\mathrm{p}} = (\Delta l/n)/l \sim 0.138$. The lateral strain is expected to be relatively small in comparison, and therefore the localized porosity reduction in the compaction bands is also inferred to be $\Delta\phi \sim 13.8$ percentage units. This value is comparable with estimates of $\Delta\phi \sim 14$–15 percentage units for discrete compaction bands in the Bentheim sandstone obtained by Baud et al. (2004) and Vajdova et al. (2004), who used a similar approach but had to infer the number $n$ of bands indirectly from the number of AE surges in the absence of direct imaging data such as Fig. 7 in this study.

The above analysis assumes that the bands are straight and exactly perpendicular to $\sigma_1$, thus neglecting the tortuosity and slight misalignment of the bands. These two effects can be estimated from our CT data. We identified 58 relatively elongate bands and determined on a 2D section (as illustrated in Fig. 6b for $X = 2.0$ mm) their curvilinear length $\ell$ and the length $L$ and dip $\theta$ of the line connecting the end points. The ratio $\ell/L$ provides a measure of the tortuosity, which has a mean value of 1.07 and a mode in the range 1.09–1.12 (Fig. 11b). The band orientation is subperpendicular to $\sigma_1$. The absolute value of the dip angle has a mean of 7° and a mode in the range 0–4° (Fig. 11c).

## 5. Summary and discussion

In this study we have developed statistical techniques that can be applied to X-ray CT data for mapping out the spatial distribution of compactant cataclastic damage due to grain crushing and pore collapse, which are difficult to resolve solely from contrasts in the X-ray attenuation. Our data show that such micromechanical processes would decrease both the skewness and dispersion of CT-values of an ensemble of voxels. Using the coefficient of variation for 27 voxels embedded in a cube with volume comparable to that of a grain, we obtain a local measure of damage that maps out the 3D geometric complexity of discrete compaction bands in the Diemelstadt sandstone. Our interpretation of the CT data was validated by microstructural observations, which also provide constraints on the binarization of CT images for quantitative
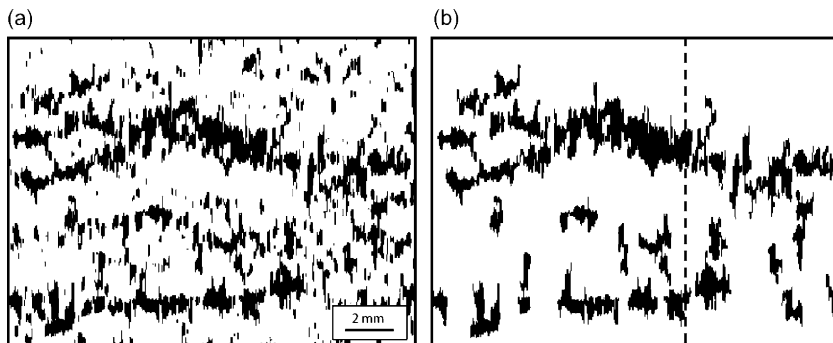


Fig. 10. (a) Section at $X = 9.1$ mm in Fig. 6b after binarization. The image was obtained using an upper threshold value of 40. (b) In order to isolate the bands, clusters smaller than 200 pixels in area are excluded from the image. Evaluation of the bands width is then automatically performed along vertical profiles (dashed line).
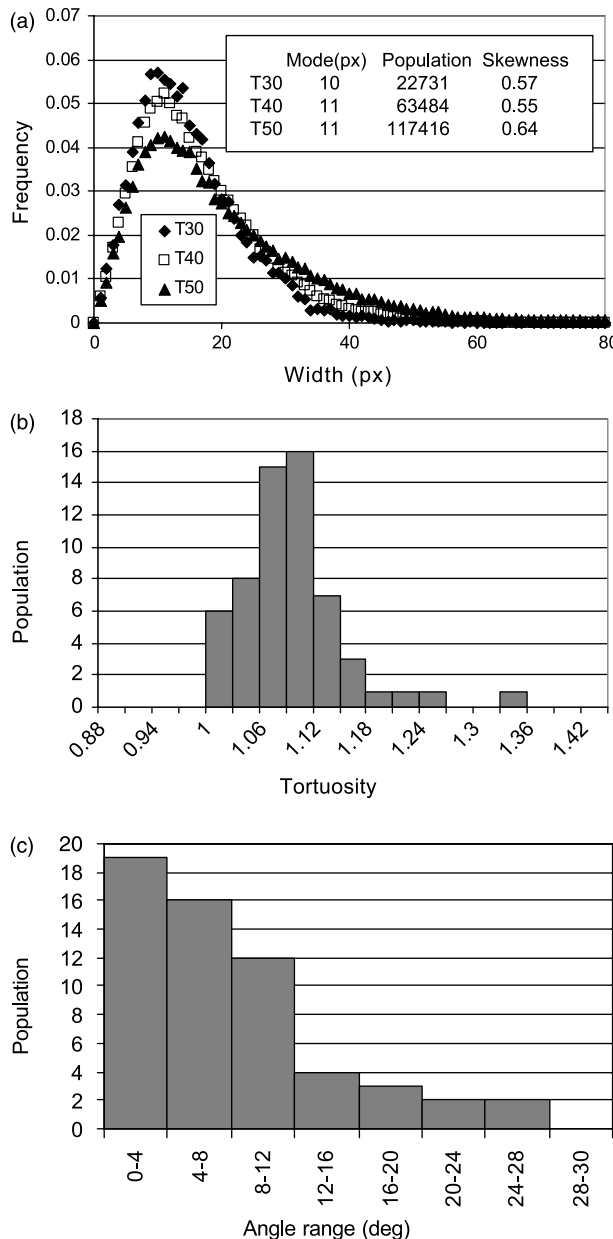
Fig. 11. (a) Evaluation of the average band thickness. The three curves are the thickness distribution corresponding to thresholds of gray level 30, 40 and 50. Despite the large range in threshold values, most frequent band width falls in the narrow range 10–11 pixels (490–540 μm). (b) and (c) Distribution of the tortuosity and orientation for 58 bands analyzed as illustrated in Fig. 6b ($X = 2$ mm). Mean tortuosity and angle are 1.07 and $-0.54°$, respectively.

characterization of the width, tortuosity, and orientation of discrete compaction bands.

If we were to depend only on a thin-section to characterize the failure mode and damage, the observation would have two limitations. First, we cannot visualize how a band propagates out of the plane of the thin-section as a curved tabular structure across the sample. Second, because it has a significant percentage of feldspar in addition to quartz, the color contrast between the crushed grains in a compaction band and the surrounding is not very pronounced (Figs. 2a and b and 8a). In contrast, Vajdova et al. (2004) were able to characterize many

geometric attributes of discrete compaction bands in Bentheim sandstone, which is made up of 95% quartz and its compaction bands made up of intensely crushed grains would show up as appreciably darker than the surrounding under the optical microscope. In our case, to map out the spatial distribution of damage (Fig. 9) would necessitate detailed stereological measurements on a thin section of the Diemelstadt sandstone, which can be very time consuming.

The geometric attributes that we obtained from our CT data show that the width and tortuosity of discrete compaction bands in Diemelstadt sandstone (Fig. 11) are quite similar to those in Bentheim sandstone, which also suggests similar effects in terms of permeability evolution associated with compaction localization (Baud et al., 2004; Vajdova et al., 2004). Our technique can potentially be applied to map out other modes of strain localization, such as diffuse compaction bands and high-angle conjugate shear bands. We note that X-ray CT technique has begun to be used on naturally deformed samples as well as core samples from scientific drilling programs, mostly focusing on characterizing the pore geometry and dilatant fault structures (e.g. Hirono, 2005; Ketcham and Iturrino, 2005). If used on such samples, the methodology developed here would broaden the scope to include the delineating of strain localization associated with compactant processes.

## 5.1. Porosity reduction and the coefficient of variation of CT-value

If our methodology were to be adopted more widely for mapping out strain localization and damage, it is necessary to first address the fundamental question: what causes the coefficient of variation $\delta$ to decrease with porosity reduction and grain crushing? There seems to be at least two causes, which are interrelated. The first was postulated by Otani et al. (2005) in the form of a heuristic model for interpreting their CT data for grain crushing in soil, which we will elaborate below and quantify using synthetic data generated from our CT measurement on Diemelstadt sandstone. With X-ray CT data are typically acquired with a fixed spatial resolution, as represented by the square windows in the 2D scenario sketched in Fig. 12a. In the compacted sample both the solid particle size and pore size were significantly reduced, and hence their dimensions have shrunk relative to the fixed window size. Otani et al. (2005) pointed out that as far as the sampling of CT data is concerned, the scenario in Fig. 12a is identical to that shown in Fig. 12b, which acquires data on a pore and grain structure that remain invariant using an expandable window of observation.

Although we did not acquire CT data using multiple spatial resolutions, the scenario shown in Fig. 12b can be simulated using synthetic data generated by our CT measurements. We have used a voxel size of $d = 48.78$ μm, but if we were to acquire our data with voxel size $nd$, the number of voxels in our core sample would be reduced by a factor of $N = n^3$. To simulate data acquisition using the coarser spatial resolution we first divide the volume into 'supervoxels' each made up of $N$ voxels, and then
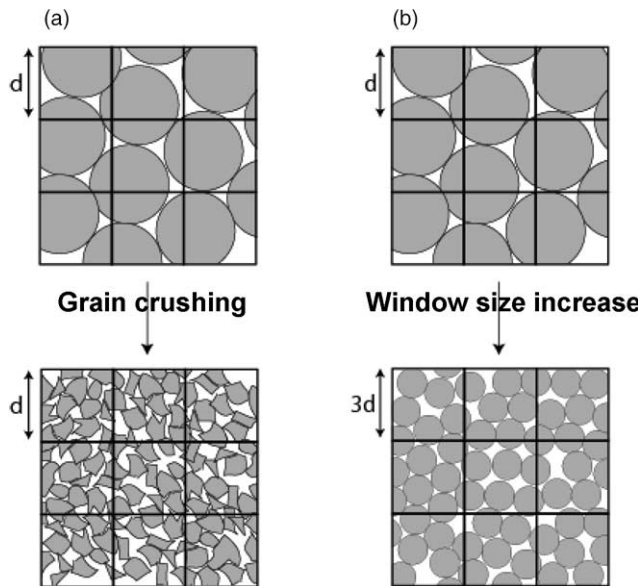
Fig. 12. (a) Sketch illustrating the effect of grain crushing on the acquisition of X-ray data using fixed size pixels. After compaction, both the solid particle size and pore size were significantly reduced; therefore their dimension has shrunk with respect to the fixed window size. (b) Conceptual equivalent of (a) suggested by Otani et al. (2005)): data are acquired on a pore and grain structure that remain invariant using an expandable window of observation.

'acquire' the CT-value for each of these supervoxels by calculating the arithmetical mean of the CT-values of the *N* voxels it encloses (Fig. 13a). Given such synthetic data on the CT-values that would be acquired at a coarser spatial resolution, we can calculate the coefficient of variation $\delta(N)$ for the slice shown in Fig. 3b. The results are given in Fig. 13b (for reference the value found in Fig. 3c for $\sigma$/mean is $\delta(1)$). There is an overall decrease of the dispersion coefficient with increasing *N*, which can be fitted empirically by $\delta(N) \propto N^{-0.135}$.

Before connecting this result to the fixed window scenario shown in Fig. 12a, it is of interest to first note that the behavior shown in Fig. 12b is in qualitative agreement with the prediction of statistical sampling theory. Indeed if the distribution is approximately normal, then it is well known in statistics that the standard deviation of the mean of a random sample of size *N* would be proportional to $1/\sqrt{N}$ (Hoel, 1962). To simulate this idealized scenario, a truly random sampling (without imposing the constraint that the *N* voxels are neighbors) was also performed in the same slice and the resulting curve (with a best fit for $\delta(N) \propto N^{-0.4782}$) was in excellent agreement with the theory. This result is for voxels that are idealized as randomly distributed, but since neighboring voxels in our sample are not independent because they may include solid material from the same grains and void space
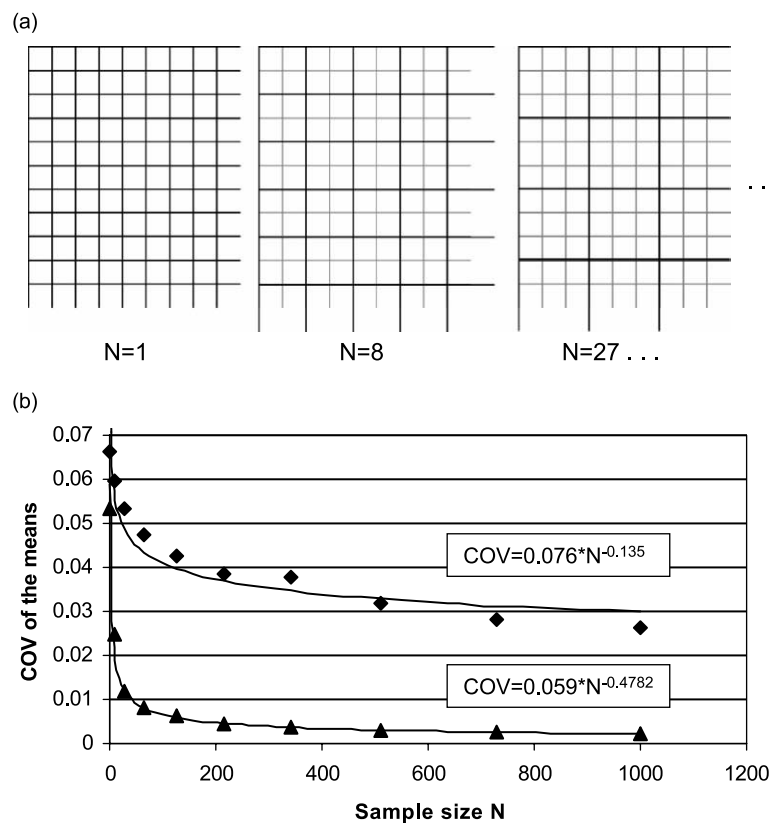


Fig. 13. (a) Procedure used to generate synthetic images that simulate acquisition of CT data with coarser resolution. The volume is first divided into 'supervoxels', then a new image is calculated attributing to each supervoxel the mean CT value of the *N* voxels it encloses. (b) Two curves showing the decrease of $\delta$ with increasing the sample size. The top curve corresponds to the evaluation of $\delta$ using the supervoxels as explained in (a). The synthetic data empirically fit a power law $\delta = 0.076N^{-0.135}$. The bottom curve was obtained also by sampling *N* pixels but they were randomly picked from all voxels within the image. This latter result agrees with the dependence on $1/\sqrt{N}$ anticipated by sampling theory.

from the same pores, it is not surprising that the decrease of $\delta$ with $N$ in the supervoxels is not as rapid as the inverse square root predicted for $N$ randomly sampled voxels. Still, the overall decrease of $\delta(N)$ with increasing voxel size is qualitatively explained and the principle could be used to smaller scales for evaluating local intensity of grain crushing and pore collapse.

If the localized deformation in a compaction band occurs simply by a self-similar shrinkage of the pore space, then the effect on the statistical variation of CT-value would be identical to increasing the window size (Fig. 12b) or voxel size (Fig. 13a). Shrinkage of the linear dimension by a factor of $1/n$ while fixing the window of observation is identical to observations of fixed pore structure while expanding the window by a factor of $n$ or increasing the number of voxels in a supervoxel by a factor of $N$. As illustrated by our synthetic data in Fig. 13b the overall effect is to reduce the coefficient of variation.

While this explains qualitatively our observation that $\delta$ was appreciably lower in compaction bands when we used a fixed voxel size, it should be noted that this idealized model of uniform shrinkage neglects a second important effect associated with compactant cataclasis. Grain crushing and pore collapse promotes relative grain movement and causes some grain particles to become more angular, and these features are not captured by the self-similar shrinkage of pore space. Indeed if the pore space did simply undergo self-similar shrinkage, the porosity and skewness would remain almost constant. The fact that appreciable porosity reduction generally occurs within compaction bands implies that particulate movement among

grains plays a dominant role during compaction localization. As indicated by our skewness analysis (Fig. 4) the cataclasis also preferentially destroyed the larger pores, thus narrowing the pore size (and CT-value) distribution and reducing the dispersion. Consequently, a damage indicator would include at the same time some information about both grain and pore size, without one being able to discriminate between these two variables.

Our analysis of the synthetic data also implies qualitative differences in the statistical distributions between medical and industrial CT. The dispersion analysis we used is viable only if the dispersion coefficient is sensitive to change in scale of either the voxels or pores, which, according to Fig. 13b, occurs when the voxel size is comparable with or smaller than the grain size. If our data were acquired using conventional medical CT typically with spatial resolution on the order of 1 mm, the voxel would enclose multiple grains and it is unlikely that the local dispersion coefficient would show appreciable changes due to compactant cataclasis. We thus have taken advantage of the significant improvement in spatial resolution in CT facilities. Indeed more details on the micromechanics of strain localization can potentially be elucidated with the use of microtomography, and such studies should be pursued in the future. However, it should also be noted that the trend shown in Fig. 13b is not expected to extrapolate all the way to μm scale. Indeed, because its spatial resolution is comparable with the scale of even the small pores, the statistics of micro-CT data would be bimodal (corresponding to mostly solid or void voxels). Specifically for the
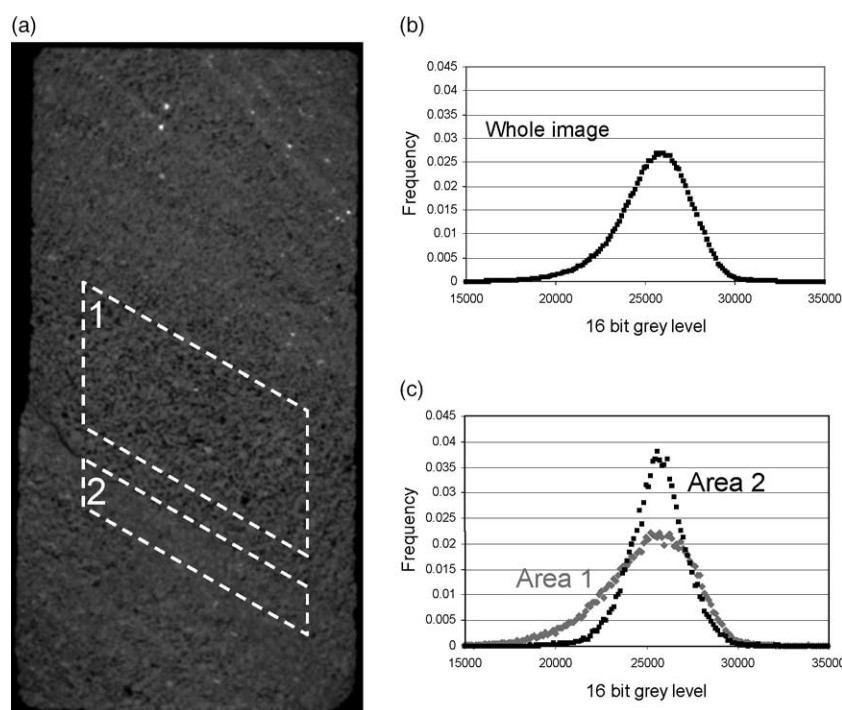


Fig. 14. (a) X-ray CT scan of a sample of Rothbach sandstone. The sample was cored at 45° with respect to the bedding. Denser areas are preexisting zones of low porosity corresponding to bedding laminae. (b) and (c) Distribution of X-ray attenuation values in areas 1 and 2. The contrast between more porous and less porous zones in terms of skewness and dispersion is greater than the one between intact and damaged zones in the Diemelstadt sandstone.

nodal pores, the recent analysis of Fontainebleau sandstone by Lindquist et al. (2000) showed that they follow a log-normal distribution.

## 5.2. Effect of initial heterogeneity

The calculation that was presented here allowed us to observe and characterize compaction bands formed in the Diemelstadt sandstone. This was made possible because a considerable contrast in homogeneity of X-ray attenuation values exists between intact and localized compacted areas. It is implicitly assumed in our methodology that the 'background' statistical variation is relatively uniform throughout an undeformed sample. While this is valid for the Diemelstadt samples we analyzed, there are a few in our block that would show very strong bedding (resolvable on conventional CT and optical microscopy observations on thin-sections) which we have excluded in this study.

It is therefore unlikely that our methodology can be applied to a rock that initially has strong heterogeneity. As an example of such a rock we present here some preliminary data on the Rothbach sandstone, which shows very strong bedding heterogeneity even under conventional CT, as illustrated in fig. 3 of Bésuelle et al. (2003). This sandstone has a porosity of 19.9% and grain average radius of 110 μm. Its modal composition is 68% quartz, 16% feldspar, 3% oxides and micas, and about 6% clays. This rock is quite unusual in that it is strongly heterogeneous in terms of local porosity. We estimated from thresholded images obtained in reflected light a variation of the 2D porosity of up to 7 percentage units from one local area to another.

Fig. 14a shows an X-ray CT scan (at a spatial resolution of 48.12 μm) of a Rothbach sandstone sample cored at 45° to the bedding plane, which is resolvable as relatively thin light bands. Fig. 14b shows the statistical distributions of CT-values (in terms of 16-bit gray levels) for the whole slice, as well as for area 1 inferred to be outside the bedding laminae and for area 2 enclosing a bedding lamina. The frequency distribution for area 2 is appreciably narrower and less skewed than in area 1, in a way similar to that in a compaction band in Diemelstadt sandstone (Fig. 3c). However, the coefficient of variation decreases from area 1 to 2 by ∼40%, which is a more significant contrast than the drop (of ∼25%) from the relatively undamaged zones to compaction bands in Diemelstadt sandstone. Since the initial heterogeneity in the undeformed sample is pronounced, it would be difficult to differentiate pre-existing bedding laminae from localized damage due to deformation in a failed sample unless these bands and other heterogeneities are imaged before and after deformation. An advantage of X-ray CT is that the imaging is nondestructive, and therefore for studying rock deformation and failure one can readily acquire the images of the same sample before and after failure for digital image correlation (Bay et al., 1999; Rechenmacher and Finno, 2004). Such an approach on imaging strain localization has just been pursued and the results are presented in a companion paper (Louis et al., submitted).

## References

Antonellini, M., Aydin, A., Pollard, D.D., d'Onfro, P., 1994. Petrophysical study of faults in sandstone using petrographic image analysis and X-ray computerized tomography. Pure and Applied Geophysics 143 (1/2/3), 181–201.

Arns, C.H., Knackstedt, M.A., Val Pinczewski, W., Martys, N.S., 2004. Virtual permeametry on microtomographic images. Journal of Petroleum Science and Engineering 45, 41–46.

Auzerais, F.M., Dunsmuir, J., Ferreol, B.B., Martys, N., Olson, J., Ramakrishnan, T.S., Rothman, D.H., Schwartz, L.M., 1996. Transport in sandstone: a study based on three dimensional microtomography. Geophysical Research Letters 23, 705–708.

Aydin, A., Borja, R.I., Eichhubl, P., 2006. Geological and mathematical framework for failure modes in granular rock. Journal of Structural Geology 28 (1), 83–98.

Baud, P., Klein, E., Wong, T.-f., 2004. Compaction localization in porous sandstones: spatial evolution of damage and acoustic emission activity. Journal of Structural Geology 26, 603–624.

Bay, B.K., Smith, T.S., Fyhrie, D.P., Saad, M., 1999. Digital volume correlation: three-dimensional strain mapping using X-ray tomography. Experimental Mechanics 39 (3), 217–226.

Bésuelle, P., Rudnicki, J.W., 2004. Localization: shear bands and compaction bands. In: Guéguen, Y., Boutéca, M. (Eds.), Mechanics of Fluid-Saturated Rocks. Elsevier, Amsterdam, pp. 219–321.

Bésuelle, P., Baud, P., Wong, T.-f., 2003. Failure mode and spatial distribution of damage in Rothbach sandstone in the brittle–ductile transition. Pure and Applied Geophysics 160, 851–868.

Borja, R.I., Aydin, A., 2004. Computational modeling of deformation bands in granular media. I: geological and mathematical framework. Computer Methods in Applied Mechanics and Engineering 193, 2667–2698.

Coles, M.E., Hazlett, R.D., Spanne, P., Soll, W.E., Muegge, E.L., Jones, K.W., 1998. Pore level imaging of fluid transport using synchrotron X-ray microtomography. Journal of Petroleum Science and Engineering 19, 55–63.

Desrues, J., Chambon, R., Mokni, M., Mazerolle, F., 1996. Void ratio evolution inside shear bands in triaxial sand specimens studied by computed tomography. Géotechnique 46 (3), 529–546.

DiGiovanni, A.A., Fredrich, J.T., Holcomb, D.J., Olsson, W.A., 2000. Micromechanics of compaction in an analogue reservoir sandstone. Proceedings of the 4th North American Rock Mechanics Symposium, 1153–1160.

Flannery, B.P., Deckman, H.W., Roberge, W.G., D'Amico, K.L., 1987. Three dimensional x-ray microtomography. Science 237, 1439–1444.

Fortin, J., Stanchis, S., Dresen, G., Gueguen, Y., accepted. Acoustic emission and velocities associated with the formation of compaction bands in sandstone. Journal of Geophysical Research accepted for publication.

Fredrich, J.T., DiGiovanni, A.A., Noble, D.R., 2006. Predicting macroscopic transport properties using microscale image data. Journal of Geophysical Research 111, B03201. doi:10.1029/2005JB003774.

Hirono, T., 2005. The role of dewatering in the progressive deformation of a sandy accretionary wedge: constraints from direct imaging of fluid flow and void structure. Tectonophysics 397, 261–280.

Hoel, P.G., 1962. Introduction to Mathematical Statistics. John Wiley & Son, New York. 427pp.

Kawakata, H., Cho, A., Kiyama, T., Yanagidani, T., Kusunose, K., Shimada, M., 1999. Three-dimensional observations of faulting process in Westerly granite under uniaxial and triaxial conditions by X-ray CT scan. Tectonophysics 313, 293–305.

Ketcham, R.A., Carlson, W.D., 2001. Acquisition, optimization and interpretation of X-ray computed tomographic imagery: applications to the geosciences. Computers and Geosciences 27, 381–400.

Ketcham, R.A., Iturrino, G.J., 2005. Nondestructive high-resolution visualization and measurement of anisotropic effective porosity in complex lithologies using high-resolution X-ray computed tomography. Journal of Hydrology 302, 92–106.

Klein, E., Reuschlé, T., 2004. A pore crack model for the mechanical behaviour of porous granular rocks in the brittle deformation regime. International Journal of Rock Mechanics and Mining Science 41, 975–986.

Lindquist, W.B., Venkatarangan, A., Dunsmuir, J., Wong, T.-f., 2000. Pore and throat size distributions measured from synchrotron X-ray tomographic images of Fontainebleau sandstones. Journal of Geophysical Research 105, 21509–21527.

Lockner, D., 1993. The role of acoustic emission in the study of rock fracture. International Journal of Rock Mechanics and Mining Science 30, 883–900.

Lockner, D.A., Byerlee, J.D., Kuksenko, V., Ponomarev, A., Sidorin, A., 1992. Observations of quasistatic fault growth from acoustic emissions. In: Evans, B., Wong, T.-f. (Eds.), Fault Mechanics and Transport Properties of Rocks. Academic, San Diego, CA, pp. 3–32.

Louis, L., Wong, T.-f., Baud, P., submitted. Imaging strain localization by X-ray computed tomography: deformation bands in Rothbach sandstone. Journal of Structural Geology.

Menéndez, B., Zhu, W., Wong, T.-f., 1996. Micromechanics of brittle faulting and cataclastic flow in Berea sandstone. Journal of Structural Geology 18, 1–16.

Mollema, P.N., Antonellini, M.A., 1996. Compaction bands: a structural analog for anti-mode I cracks in aeolian sandstone. Tectonophysics 267, 209–228.

Olsson, W.A., Holcomb, D.J., 2000. Compaction localization in porous rock. Geophysical Research Letters 27, 3537–3540.

Otani, J., Mukunoki, T., Sugawara, K., 2005. Evaluation of particle crushing in soils using X-ray CT data. Soils and Foundations 45, 99–108.

Paterson, M.S., Wong, T.-f., 2005. Experimental Rock Deformation—The Brittle Field, 2nd ed Spinger-Verlag, New York.

Raynaud, S., Fabre, D., Mazerolle, F., Geraud, Y., Latiere, H.J., 1989. Analysis of the internal structure of rocks and characterization of mechanical deformation by a non-destructive method: X-ray tomodensitometry. Tectonophysics 159, 149–159.

Rechenmacher, A.L., Finno, R.J., 2004. Digital image correlation to evaluate shear banding in dilative sands. Geotechnical Testing Journal 27 (1), 13–22.

Renard, F., Bernard, D., Thibault, X., Boller, E, 2004. Synchrotron 3D microtomography of halite aggregates during experimental pressure solution creep and evolution of the permeability. Geophysical Research Letters 31, L07607. doi:10.1029/2004GL019605.

Segall, P., Pollard, D.D., 1983. Nucleation and growth of strike-slip faults in granite. Journal of Geophysical Research 88, 555–568.

Tapponier, P., Brace, W.F., 1976. Development of stress-induced microcracks in Westerly granite. International Journal of Rock Mechanics and Mining Science 13, 103–112.

Vajdova, V., Baud, P., Wong, T.-f., 2004. Permeability evolution during localized deformation in Bentheim sandstone. Journal of Geophysical Research 109, B10406. doi:10.1029/2003JB002942.

Vinegar, H.J., De Waal, J.A., Wellington, S.L., 1991. CT studies of brittle failure in castlegate sandstone. International Journal of Rock Mechanics and Mining Science 28 (5), 441–448.

Wellington, S.L., Vinegar, H.J., 1987. X-ray computerized tomography. Journal of Petroleum Technology 39, 885–898.

Willemse, E.J.M., Peacock, D.C.P., Aydin, A., 1997. Nucleation and growth of strike-slip faults in limestones from Somerset, U.K.. Journal of Structural Geology 19, 1461–1477.

Wong, T.-f., 1982. Micromechanics of faulting in Westerly granite. International Journal of Rock Mechanics and Mining Science 19, 49–64.

Wong, T.-f., David, C., Zhu, W., 1997. The transition from brittle faulting to cataclastic flow in porous sandstones: mechanical deformation. Journal of Geophysical Research 102, 3009–3025.